



Proper orthogonal decomposition of straight and level flight kinematics in an insectivorous bat

Xiaozhou Fan, Peter Windes, Danesh Tafti, Susheel Sekhar, Matt Bender,
 Andrew Kurdila and Rolf Müller
 Department of Mechanical Engineering
 Virginia Tech, Blacksburg, VA, 24061

The kinematics of hipposiderid bats (*Hipposideros pratti*) in straight and level flight has been deconstructed into a series of modes using proper orthogonal decomposition, to determine the relative importance of each mode in the overall force dynamics. Simplified kinematics have been reconstructed using different combinations of modes, and large eddy simulations were performed to compare the forces generated for each case. The first two modes (0,1) recovered only 62% of the lift, and manifested a drag force instead of thrust, whereas the first three modes (0,1,2) recovered 77% of the thrust and, unexpectedly, even more lift than the native kinematics. This demonstrates that mode 2, which features a combination of streamwise and chordwise cambering and twisting during the upstroke, is critical for the generation of lift, and more so for thrust. Detailed flow analyses reveal that the leading edge vortex and the trailing edge vortex hold the key to understanding this phenomenon. Such reduced order modeling of bat flight could provide guidelines for designing autonomous micro air vehicles which require a detailed understanding of the associated forces for the preservation of structural integrity.

Nomenclature

\mathbf{X}	= data matrix
\mathbf{S}_x	= covariance matrix of data matrix
\mathbf{U}	= orthonormal eigenvectors of covariance matrix
Σ	= eigenvalue sets of covariance matrix
\mathbf{Y}	= transformed data matrix having a diagonal covariance matrix
$\tilde{\mathbf{X}}$	= truncated data matrix
$\tilde{\mathbf{S}}_x$	= truncated covariance matrix
ρ	= density of air
U_{ref}	= reference velocity
L_{ref}	= chord length of the bat
q	= dynamic pressure
t^*	= nondimensional time
t_{ref}	= reference time

I. Introduction

Though less efficient than birds at flying long distances¹, bats excel at maneuvering flight as they possess highly articulated skeletal structures with pliant membranous covers that act as flexible aerodynamic control surfaces². While flapping-wing micro aerial vehicles (MAVs) that mimic birds and insects have been extensively researched and adapted to miniaturized flying devices^{3,4}, equivalent studies and efforts for bat flight⁴⁻⁶ have seen very few practical implementations. One major roadblock in this effort is the absence of simulation tools in the design loop^{7,8} that can feed force data back into flight aerodynamics.

Recent advances in motion capturing technology⁹ have enabled detailed studies of bat flight. Tian *et al.*¹⁰ experimentally measured the wing kinematics using around 20 reflective markers on the left wing in straight and turning flight, and performed a simple analysis of the wake structure for straight flight. However, their estimated lift using PIV-derived wake data (17gms) could only account for less than half of the bat's weight (~40gms). This left a significant portion of the lift force, and its associated dynamics, unaccounted for. Nevertheless, this was the first quantitative experimental study that utilized advances in modern wind tunnel technology and recent developments in flow visualization techniques for bat flight¹¹. Muijre *et al.*¹² showed that a slow flying bat (*Glossophaga soricina*) uses an attached leading edge vortex (LEV) to generate 40% of the lift, using DPIV-derived data. Hubel *et al.*¹³ used a similar experimental approach with 5 markers on the right side of the bat to reveal four typical vortical structures across different flight speeds. They discovered that the presence of a tip vortex is not constant at high speeds, which contrasts the continuous vortical structure found in bird flight. Subsequently, Hubel *et al.*¹⁴ compared the kinematics of two insectivorous bats (*Tadarida brasiliensis* and *Myotis velifer*) using 5 markers on the right side of the bats, and showed that they differ significantly in prey pursuit at slow flight. They inferred that *M. velifer* has a better flight efficiency for two reasons: a decreased disruption in lift generation between the body and wing, and a characteristic root vortex with diminishing strength. They also concluded that generalizations about bat aerodynamic performances should be made with proper considerations. Bender *et al.*^{9,15} used a much higher density of marker distribution (up to 200 markers on both of the bat wings), which allowed them to extract a more accurate description of the bat wing in motion. Their motion capturing system consisted of a large three-dimensional array of 21 GoPro HERO3+ Black action cameras (720p at 120fps) arranged along the walls of a rectangular flight tunnel. Wing kinematics of an insectivorous bat species, Pratt's roundleaf bat (*Hipposideros pratti*), were obtained. Due to the high fidelity of the experimental data from this setup, it has been used to prescribe the trajectory for a bat model in this study.

Pivkin *et al.*¹⁶ were the first to simulate bat flight numerically. In their effort, the wing of a bat (*Pteropus poliocephalus*) was represented by an infinitesimally thin tessellation of triangles using around 22 markers placed on the body and bones structures. They simulated a low Reynolds number ($Re = 100$) test flight using an arbitrary Lagrangian-Eulerian (ALE) method, and visualized the resulting flow patterns. Wang *et al.*¹⁷ used an immersed boundary method (IBM) strategy to simulate a slow flying bat ($Re = 1000$). The wing outline was obtained using 5 markers on a flying fox in maximum wingspan (*Pteropus poliocephalus*), and this outline was driven by the wing kinematics of another bat species, the Pallas long-tongued bat (*Glossophaga soricina*). The results from their direct numerical simulation (DNS) compared well with PIV results of the same bat flight kinematics. It should be noted here that the data for their experiments were obtained from a motion capturing setup with only five markers on the bat wing, with the rest of the kinematics being interpolated. Viswanath *et al.*¹⁸, on the other hand, simulated the straight, climbing flight of a species of fruit bat (*Cynopterus brachyotis*) using a similar IBM strategy. The kinematics of a single wing with 50 markers was modified into a periodic motion to ensure fully developed flow at two different Reynolds numbers (433 and 5625), and the visualized flow structures were used to gain a detailed insight into the effect of the LEV on the generated lift and thrust. Nondimensional lift and drag forces were found to be independent of the Reynolds number in these simulations. Additionally, they showed that by decomposing the kinematics using proper orthogonal decomposition (POD) into the sum of a collection of movements, merely two movements (or modes) could explain almost all of the resulting averaged forces. Though their decomposition of wing kinematics was based on a single wing, the overall strategy offers excellent potential to choose important kinematics in designing flapping wing MAVs based on bat flight data.

In this paper, we present a data pre-processing strategy for conditioning the experimental data obtained through motion capture to make it suitable for aerodynamic simulations. POD combined with data imputation is used to deconstruct the full wing kinematics into a series of modes representing the native kinematics. The most energetic modes are discussed in some detail. Aerodynamic simulations are then used to investigate the effect of mode combinations on the ensuing unsteady flow field generated by the wing, and on force production. It is shown that POD analysis with data imputation can be used as an effective tool for pre-filtering the raw motion capture data without any loss in meaningful content.

II. Methodology



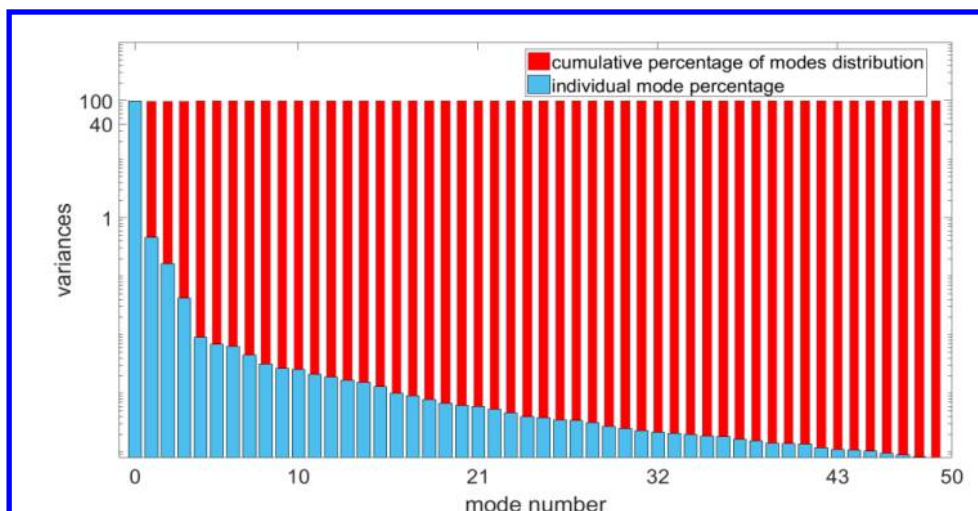
Figure 1. Motion capture experimental setup.

A. Experiment setup

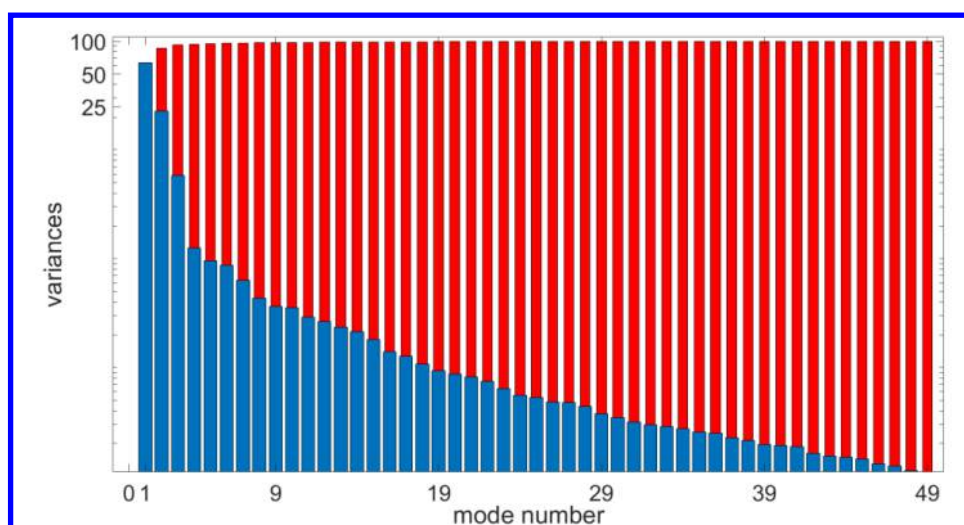
The experimental subjects for this study were 8 adult specimens of Pratt's roundleaf bat, 6 males and 2 females. The animals were kept in indoor aviaries, and put on a diet of mealworms and water provided *ad libidum*. The experiments were conducted in a tunnel with dimensions $1.12\text{m} \times 1.12\text{m} \times 5\text{m}$, in which the bats were made to fly the length of the tunnel. The flights were captured by 21 synchronized high-speed video cameras (GoPro Hero 3+ Black), with the resolution set to 1280×720 (720p) and the frame rate set to 120 fps. The cameras were arranged on the walls of a tubular flight tunnel, as shown in Figure 1(c) in order to observe the flying bat from various viewing directions. About 150 small round marker points were painted onto the bats' wings using a non-toxic paint to facilitate tracking (Figure 1(a) and (b)). An example of high-speed video frames overlaid on each other is shown in Figure 1(d). The methods used for correlating the motion capture data between different cameras to obtain the trajectory of each marker point in space and time are outlined in Bender *et al.*⁹

B. Pre-processing of Motion Capture Data and Educing Native Kinematics

Processing the motion capture data to build a mathematical model for the wing kinematics, and a three-dimensional mesh of the wing for use in a computational fluid dynamics (CFD) simulation, poses a number of challenges. Typically, the recorded field data contains data inconsistencies due to issues with the recorded image data. These inconsistencies are in the form of occlusions (missing data), as well as spatial and temporal discontinuities in the raw recorded data. Pre-processing is an essential step to close gaps in the data set, and to filter out erroneous points.¹⁸



(a) Variances of each mode including the translational motion (mode 0) of the bat



(b) Variances of each mode excluding the translational motion (mode 0) of the bat

Figure 2. Variances of each mode and cumulative distribution

During the experiment, the bat wings were subjected to a high degree of flapping and twisting, which could result in certain feature points not being seen by more than one camera. Since two cameras are needed at minimum to perform triangulation, a number of observations could result in void entries. Another source of error in the data is the precision of the stereo-triangulation. A feature point observed by two cameras close to each other can display a large degree of range ambiguity. Additionally, incorrect association of marker points between cameras, and errors in the cameras' extrinsic/intrinsic parameters, can result in outliers appearing in the final marker point data set. These errors must be properly addressed before the kinematics data can be used in CFD analyses.

In the pre-processing step, void entries in the data set were interpolated in time from adjacent frames showing the respective landmarks by virtue of piecewise cubic splines¹⁹. For void entries that could not be interpolated (occlusion at the beginning or the end of frame sequences), data imputation was used, which takes into account not only information regarding the observation of missing values and the values themselves, but also considers their relationship with the rest of the observations and values. For this, we used the trimmed scores regression (TSR) method introduced by Folch-Fortuny *et al.*²⁰ This was combined with POD. In the current context, the POD was not only used to deconstruct the wing motion into its most energetic components, it also served as a pre-filter to eliminate spurious noise from the wing kinematics. This was done under the implicit assumption that spurious noise in the measured

kinematics is associated with modes that contain less energy overall, but could nevertheless have a detrimental effect on the stability of aerodynamic simulations.

C. Proper Orthogonal Decomposition

Proper orthogonal decomposition (POD), commonly known in statistics as principal component analysis (PCA) finds a transformation, \mathbf{P} , that acts on data matrix, \mathbf{X} , so that the resulting matrix, $\mathbf{Y} = \mathbf{P} \mathbf{X}$, will have a diagonal covariance matrix, \mathbf{S}_Y . If the off-diagonal elements in \mathbf{Y} are zero, then the new variables are independent of (or orthogonal to) each other, *i.e.*, a change in one variable will have no impact on the values of the others. Furthermore, the transformation matrix, \mathbf{P} , can be shown to be the eigenvector of the covariance matrix, \mathbf{S}_X , of \mathbf{X} , and the corresponding eigenvalues are the weight (or energy content²¹) of each eigenvector. Note that the extracted modes are still a linear projection of the actual motion, and hence, any nonlinear phenomenon analyzed using POD will have limitations²². The covariance data matrix, \mathbf{S}_X , for the data matrix, \mathbf{X} , can be written as:

$$\mathbf{S}_X = \sigma_0 \mathbf{u}_0 \otimes \mathbf{u}_0 + \sigma_1 \mathbf{u}_1 \otimes \mathbf{u}_1 + \sigma_2 \mathbf{u}_2 \otimes \mathbf{u}_2 + \sigma_3 \mathbf{u}_3 \otimes \mathbf{u}_3 + \dots + \sigma_n \mathbf{u}_n \otimes \mathbf{u}_n \quad (1)$$

where, $\mathbf{U} = [\mathbf{u}_0 \ \mathbf{u}_1 \ \mathbf{u}_2 \ \mathbf{u}_3 \dots \mathbf{u}_n]$ is the orthonormal eigenvector set of \mathbf{S}_X , and $\mathbf{\Sigma} = [\sigma_0 \ \sigma_1 \ \sigma_2 \dots \sigma_n]$ is the corresponding eigenvalue set, with $\sigma_0 \geq \sigma_1 \geq \sigma_2 \geq \dots \geq \sigma_{n-1} \geq \sigma_n$, with n being the number of modes.

Consider the first term, $\tilde{\mathbf{S}}_X = \sigma_0 \mathbf{u}_0 \otimes \mathbf{u}_0$: this is one part of the variance, and it corresponds to a data matrix $\tilde{\mathbf{X}}_X = \frac{1}{m-1} \mathbf{x}_0 \mathbf{x}_0^T$, where \mathbf{x}_0 is a subsystem that is an approximation of the original \mathbf{X} , in the sense that it accounts for $\tilde{\mathbf{S}}_X = \sigma_0 \mathbf{u}_0 \otimes \mathbf{u}_0^T$ amount of variance, with σ_0 being the maximum eigenvalue. This \mathbf{x}_0 corresponds to mode 0. Similarly, subsequent modes 1, 2, ..., n can be constructed.

Figure 2 plots the variance of each mode in the data set on a log-scale. Figure 2(a) includes the translation mode (mode 0) which dominates the full motion, whereas Figure 2(b) excludes it. By assuming outliers to be eigenvectors associated with small eigenvalues, a truncated data matrix was reconstructed by considering only the eigenvectors

Table 1 Mode variance distribution

First k modes	2	3	5	6	7	8	10	11	14	20	30
Cumulative variance (%),including 0-th mode	99.7376	99.9024	99.9535	99.9604	99.9667	99.9744	99.9770	99.9796	99.9853	99.9915	99.9958
Cumulative variance (%),excluding 0-th mode	63.8361	86.6532	93.7276	94.6870	95.5577	96.1895	96.9900	97.6360	98.1348	98.9951	99.5800

corresponding to large eigenvalues. Mode 0, which is a rigid body-like translational motion of the bat, accounted for more than 99% of the variances, followed by modes with progressively decreasing energy content. If the translation mode, mode 0, was excluded from the modal analysis, modes 1 and 2, which are more relevant to the wing flapping motion, collectively contributed 63.84% to the full kinematics, as shown in Table 1. This cumulative contribution increased to 95% when only the first 7 flapping modes were included in the kinematics, and to 99.96 % when the translational motion of the bat were also included.

1) Modes 0 + 1

A combination of the first two modes (0 and 1) results in a kinematics matrix, $\mathbf{X} = (\mathbf{x}_0 + \mathbf{x}_1)$. Four snapshots in time of the bat following this flight path are shown in Figure 3(a). The wingtip trajectories are also plotted, and the body is approximated as an ellipse to visualize orientation. The length of the black arrows denotes the velocity magnitude, and the pink transparent box delineates the distance traversed in the X, Y and Z directions. The first snapshot is the instant when the wing is in the middle of the downstroke, and the second shows the end of it. The third continues to the middle of the upstroke, and the fourth plot completes one flapping cycle. The combination of modes 0 and 1 results in the wingtip points tracing sinusoidal curves along two nearly parallel planes. Also noteworthy is that for snapshots 2 and 4, namely during the downstroke, the velocity magnitudes are larger than those for snapshots 1 and 3.

2) Modes 0 + 1 + 2

Combining the first three modes (0+1+2) results in a different kinematics matrix, $\mathbf{X} = (\mathbf{x}_0 + \mathbf{x}_1 + \mathbf{x}_2)$, shown in Figure 3(b). Significant differences between these two combinations are evident in the third snapshot, in the middle of the upstroke: here, the wing is folded inward, thrown forward, and twisted along the wingspan. This is also apparent in the trajectory of wingtip points.

3) Modes 0 + 1 + 2 + 3 + 4 + 5 + 6

Combining the first seven modes (0+1+2+3+4+5+6) results in a new kinematics matrix, $\mathbf{X} = (\mathbf{x}_0 + \mathbf{x}_1 + \mathbf{x}_2 + \mathbf{x}_3 + \mathbf{x}_4 + \mathbf{x}_5 + \mathbf{x}_6)$, shown in Figure 3(c). There were no apparent differences between this combination and for modes (0+1+2). Thus, it is surmised that higher modes may not contribute substantially to the kinematics, and could be neglected. This is validated by aerodynamic simulations in the next section.

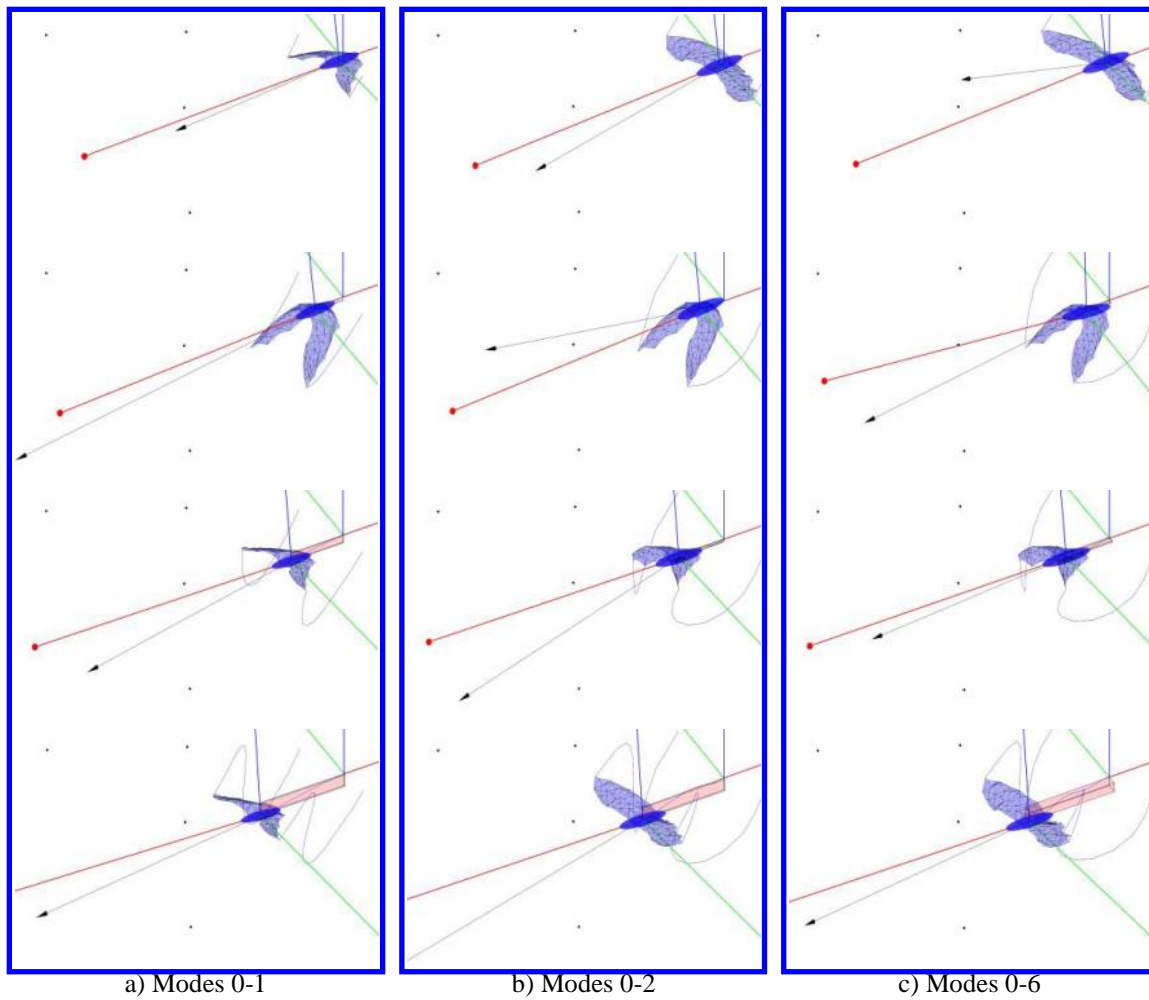


Figure 3. Kinematics of combinations of modes

4) Filtered native wing kinematics

As noted previously, the native measured kinematics can contain sudden localized temporal spatial jumps in one or two feature points due to measurement errors. While these localized discontinuities may not contribute to force production, they can have detrimental effects on the stability of the aerodynamic simulation. It is hypothesized that these spurious discontinuities manifest themselves in the low energy modes of a POD decomposition, and thus can be eliminated from the wing kinematics by using truncated POD modes to describe the native kinematics. The modes described in the previous section were solely obtained from the measured kinematics. However, no determination was made as to how these modes relate to the force dynamics generated by the wing. In this section, aerodynamic

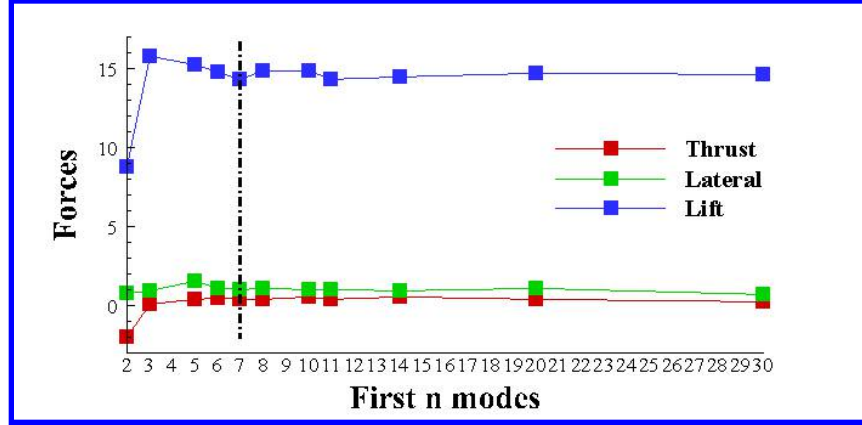


Figure 4. Comparison of average force production over three flapping cycles by including the first n POD modes in describing the kinematics. The forces are normalized by $(\rho U_{ref}^2 L_{ref}^2)$. In all simulations, $L_{ref} = 0.07\text{m}$, corresponding to the maximum chord length and the average freestream velocity is $U_{ref} = 2.8\text{m/s}$.

simulations are conducted by including the first n modes to determine their impact on force production. In particular, it is to be established that only the first few most energetic POD modes are necessary to represent the native kinematics. This can be shown by establishing that the force production asymptotes to near constant values with the inclusion of more modes.

Unsteady aerodynamic simulations were conducted to calculate the dynamic forces generated by the flapping wing using an immersed boundary method. These simulations were performed over three flapping cycles of the bat as captured by the experiments. Details of the governing equations, numerical method, geometry, boundary conditions, surface and volume grid resolution, and grid independence study are given in the following Numerical Setup section. Figure 4 shows the variation of the cycle averaged forces for the first n POD modes being used to describe the kinematics. Note that $n=2$ refers to modes 0+1, $n=10$ refers to modes 0-9, and so on. Thus, 11 separate unsteady aerodynamic calculations up to $n=30$ were done to construct Figure 4, each over three flapping cycles, with different truncated kinematics characterized by the first n POD modes. Three characteristic normalized forces are plotted: the lift force, drag force, and the lateral force. Since the translational velocity of the bat accelerates slightly over the three flapping cycles, the resultant thrust force settles to a very small value of ~ 0.5 , whereas the lateral force asymptotes to ~ 1.0 , which is in agreement with the observed trajectory of the bat.

It can be seen that there is a sharp change in the force magnitudes when going from $n=2$ to 3, but the forces quickly settle down to a near constant value after $n=6$, with small changes after that. This affirms the hypothesis that force production is dominated by the most energetic modes, and using a truncated POD modal series does not impact the dynamics. Thus, in the present work, a series containing up to seven POD modes ($n=7$) has been taken to be representative of the native kinematics.

D. Numerical Setup

1) Governing Equations

All the calculations were performed using an in-house developed code, GenIDLEST²³ (Generalized Incompressible Direct and Large Eddy Simulation of Turbulence). It is a parallelized solver developed for time-dependent fluid flow and heat transfer calculations. GenIDLEST solves the incompressible Navier-Stokes equations (Eqns. 2 and 3) in the generalized coordinate framework. More details about the formulation can be found in Ref. 24.

$$\frac{\partial u_i}{\partial x_i} = 0 \quad (2)$$

$$\frac{\partial u_i}{\partial t} + \frac{\partial}{\partial x_j} (u_i u_j) = -\frac{\partial p}{\partial x_i} + \frac{\partial}{\partial x_j} \left[\left(\frac{1}{Re} + \frac{1}{Re_t} \right) \frac{\partial u_i}{\partial x_j} \right] \quad (3)$$

where the state variables are non-dimensionalized as:

$$x_i = \frac{x_i}{L_{ref}}; u_i = \frac{u_i}{u_{ref}}; t = \frac{t}{L_{ref}}; p = \frac{p - p_{ref}}{\rho_{ref} u_{ref}^2}; Re = \frac{\rho_{ref} u_{ref} L_{ref}}{\mu_{ref}}$$

Here, the superscript ‘*’ and the reference parameters are dimensional quantities. In the present work, $L_{ref} = c$, the maximum wing chord = 0.07m*, and $u_{ref} = 2.8$ m/s, the average flight velocity, p_{ref} is the atmospheric pressure, and $\rho_{ref} = 1.25$ kg/m³. Note that a previous study²⁵ showed that the nondimensional forces (lift, thrust, *etc.*) are independent of the Reynolds number under these conditions, and considering the fact that at low Reynolds numbers, flows display more well-defined large steady structures, we therefore increased μ_{ref} to $\mu_{ref} = 6.2 \times 10^{-4}$. Thus, $Re = \frac{\rho_{ref} u_{ref} L_{ref}}{\mu_{ref}} = \frac{1.25 \times 2.8 \times 0.07}{6.2 \times 10^{-4}} = 395$. Re_t is the turbulent Reynolds number based on the subgrid turbulent viscosity, which is calculated using the dynamic Smagorinsky subgrid scale model²⁶.

The above equations were transformed to generalized coordinates, and solved using a conservative finite-volume formulation on a non-staggered grid topology. The Cartesian velocities, pressure and temperature were calculated and stored at the cell center, whereas the contravariant mass fluxes were calculated and stored at the cell faces. For time integration, a projection method using second order predictor-corrector steps was used. The predictor step calculates an intermediate velocity field, and the corrector step calculates the updated divergence free velocity at the new time-step by solving a pressure-Poisson equation. A second-order central difference operator were used for the convection and diffusion terms. Linear systems resulting in the implicit treatment of the momentum and energy equations, and the solution of the elliptic pressure equation are solved using a preconditioned BiCGSTAB method.

The bat wing was represented in the calculations as a moving immersed surface in a volumetric background mesh using an indirect forcing sharp-interface immersed boundary method (IBM) for infinitesimally thin surfaces. The wing surface, which comprises the fluid-solid interface, was defined by a triangulated surface mesh in which each surface element or cell is defined by an outward pointing unit normal, element vertices, and element centroid. Surface element values of flow variables were defined at the centroids. For the wing in motion, the fluid-solid interface was tracked in the flow at each time step. Based on the location of the boundary, all the nodes in the background volume mesh were designated as ‘‘fluid nodes’’ on the fluid side of the interface, ‘‘solid nodes’’ on the solid side of the interface, and ‘‘fluid IB nodes’’ directly adjacent to the interface on the fluid side. In the thin surface implementation, there are no solid nodes.

Boundary conditions at the IB surface were implemented by defining ‘‘probes’’ along the surface normal passing through the fluid IB nodes. The flow variables were interpolated from the surrounding fluid nodes at the probe location using tri-linear interpolation. Using this value and the appropriate boundary condition (Dirichlet or Neumann) at the IB surface, a representative value of the fluid IB node was obtained. Subsequently, the fluid IB nodes were used to provide boundary conditions for the solution at the fluid nodes. The node identification procedure and implementation of boundary conditions are described in detail in Nagendra *et al.*²⁷. It has been shown that the IBM maintains second-order accuracy.

2) Fluid Domain and Boundary Conditions

The computational domain, shown in Figure 5 consisted of a rectangular channel (1.12m×1.12m cross-section, and 2.1m in the streamwise direction) representing the experimental flight tunnel. In normalized form, the dimension of the computational domain was 30×16×16 wing chords (along the streamwise, lateral and vertical directions, respectively). Along the streamwise direction, from the inlet to the outlet, the background mesh was divided into three sections, as shown in Figure 5: (i) a relatively coarse section that extends 7 chord-lengths, (ii) a refined section around the bat geometry to resolve the flow around the wings that extends 7 chord-lengths, which is represented by the black box, and (iii) a long coarsened section leading to the outlet that extends 16 chord-lengths. A similar strategy was applied to the y and z directions. A total of 31.4 million background grid-cells were used.

Inlet and outlet boundary conditions were specified along the inflow and outflow planes, respectively. A moving frame of reference was used in which the coordinate frame is attached to the bat with an inlet air velocity of 2.8m/s. The

*The chord length is defined as the ratio of the maximum tip-to-tip planform area subtended by the bat and the tip-to-tip wingspan.

sidewalls of the tunnel are given a slip velocity equal to the inlet velocity. A zero gradient condition was specified at the outlet of the domain.

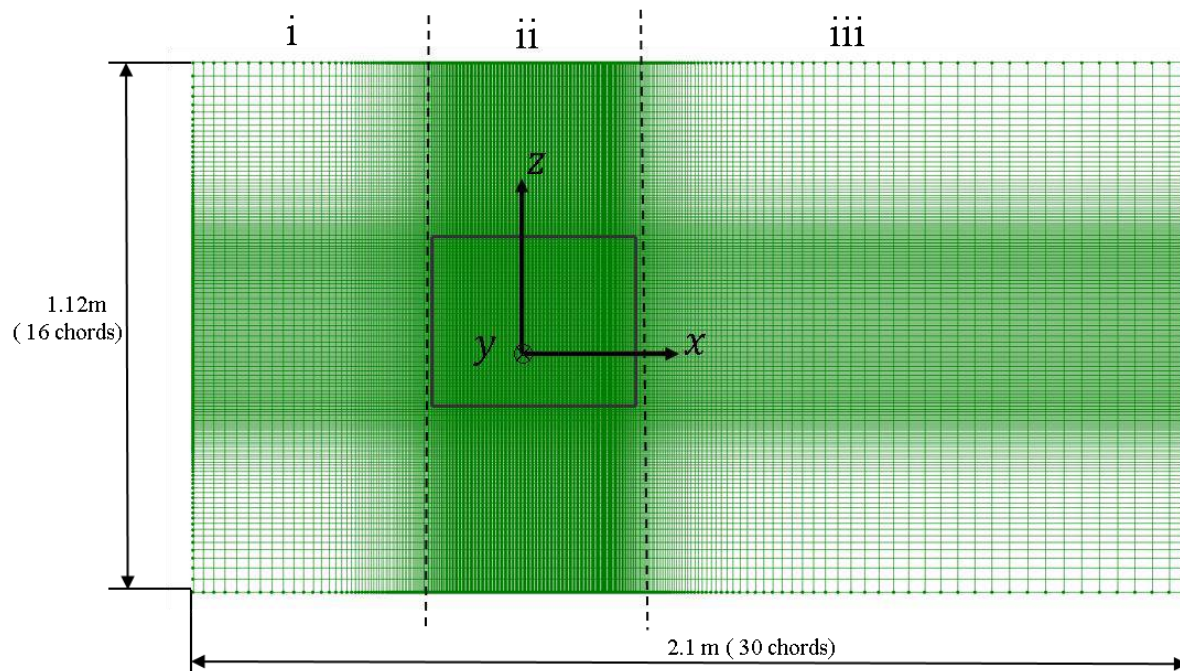


Figure 5. Background mesh for the fluid simulation. Enclosed area represents the bat location.

Each calculation used 128 cores on the Cascades cluster at Virginia Tech's Advanced Research Computing facility, and took approximately 40 hours of wall clock time for simulating the measured flight path of the bat, with a time step of approximately 25 microseconds.

3) Representation of Flapping Wing

From the wing kinematics of interest, a coarse discrete space-time (x,y,z,t) representation of each marker or feature point was available, which needed to be transformed into a space-time surface for aerodynamic simulations. To accomplish this, the measured experimental feature points or "control points" were used as the basis to generate a wing surface. Every control point corresponded to a marker physically painted on the wing. To get the surface mesh of the wing, control points that were on the bones of the bat wings were first identified and connected to set constraints for the mesh, and then Delaunay triangulation was performed to connect all control points on the wing membrane. This initial mesh, however, was much too coarse for aerodynamic simulations. To limit numerical discretization errors, and to maintain compatibility with the background grid, the wing has to be resolved on a much finer scale both spatially and temporally. Thus, each control triangle was further refined using the commercial software Pointwise, resulting in a finer mesh where each element edge length was of the order of the cell length in the background fluid mesh. The fine interpolated mesh, together with the coarser control points, is illustrated in Figure 6.

The fluid simulation only realizes the fine mesh, while the movement algorithm for the wing surface was linked to the coarse mesh. The location of each fine mesh vertex within a given control triangle can be described as a linear combination of two parameters (a,b) , both ranging between 0 and 1. The fine mesh was generated based on the initial position and the shape of the wings. The (a,b) values were calculated once, and remained constant as the wing moves. That is, the interior points maintain their relative positions with respect to the vertices of the control triangles as the wing moves. The total number of fine nodes constituting the surface mesh was approximately 50,000.

The movement of the immersed surface mesh was defined by piecewise cubic splines in an analytic form that describe the continuous evolution of each control point in time. Thus, each cubic spline can be evaluated at any given time.

Subsequently, all interior points were iterated through and updated based on their respective stored (a,b) values, as well as the updated control point locations.

In the IBM implementation²⁷, once the wing mesh reaches its new location at the next time step, the centroid of each surface element is located on the computational grid using a search algorithm – that is, the element's computational (i,j,k) coordinates are determined using its (x,y,z) location. This allows for proper data exchange between the fluid and wing surface to ensure that the existence of the wing is manifested in the fluid field. The wing surface velocity was calculated for each element using a second order backwards difference scheme in time. Similarly, the wing acceleration was calculated using the second time derivative of the surface element locations. The surface element velocities impact the fluid momentum equations, while the element accelerations impact the solution of the pressure equation.

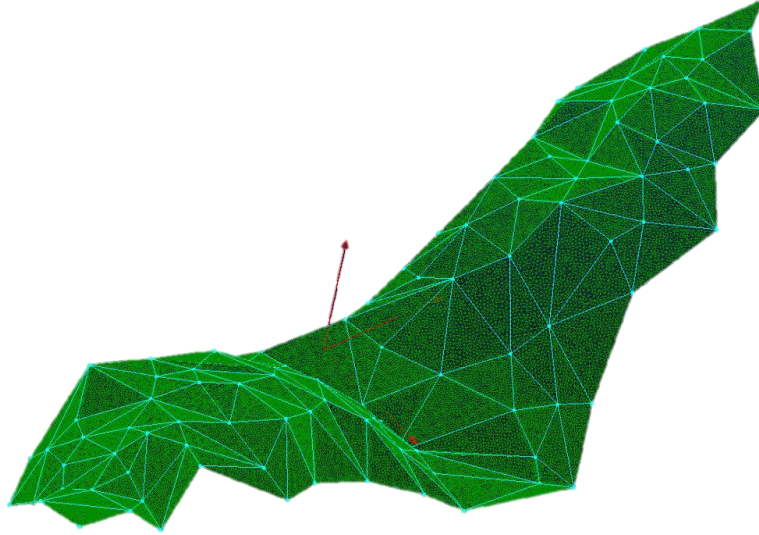


Figure 6. Surface mesh of bat wing showing fine cells

III. Result and discussion

A. Grid Independence Study

A grid independence study was carried out by using four different Cartesian background grids ranging from 20 to 70 million background computational cells, while keeping the wing surface grid the same. In all cases, the native kinematics comprising of the first 7 POD modes was used. The results are shown in Table 2. The averaged differences E_i of forces F_i (thrust, lateral and lift force) from different grids were calculated using:

$$E_i = \frac{1}{n_2 - n_1} \sum_{n=n_1}^{n_2} \frac{|F_{i,n} - \hat{F}_n|}{|\hat{F}_n|} \times 100\%, \quad (4)$$

Table 2 Grid independence study

Total number of cells	Edge length (δ) in the refined region	Aspect ratio of cell in the refined region ($\delta_x : \delta_y : \delta_z$)	E_1 (Thrust)	E_2 (Lateral)	E_3 (Lift)
20×10^6	1/28	1:1:1	0.0478%	1.6338%	0.2710%
32×10^6	1/36	0.67:0.72:1	0.0326%	1.1550%	0.0519%
45×10^6	1/36	1:1:1	0.0093%	1.1471%	0.0534%
70×10^6	1/50	1:1:1	-	-	-

where i is an index for the x, y, z component of the force, and n stands for the timestep. \hat{F}_n is the baseline force calculated on the 70 million cells mesh. It has been shown that the forces are grid independent for all the grids tested, with a maximum difference of 1.6% in the lateral force for the 20 million cells mesh. Based on these results, all calculations were done on the 31.4 million cells mesh.

B. Effect of POD modes on unsteady force production

To take a closer look at the trends in the cycle-averaged forces shown in Figure 4, the instantaneous normalized lift, thrust, and lateral forces are plotted in Figure 7 against normalized time over three flapping cycles, for $n=2$, $n=3$ and $n=7$, the native kinematics. The forces have been normalized by $\rho U_{ref}^2 L_{ref}^2$, whereas time has been normalized using the reference time scale ($t_{ref} = L_{ref}/U_{ref}$). In all these simulations, $L_{ref} = 0.07\text{m}$, which is the chord length of the bat wing, and $U_{ref} = 2.8\text{m/s}$, the average freestream velocity.

The averaged forces associated with modes 0+1+2 are similar to those of the first 7 modes. However, significant differences are evident between modes 0+1 and modes 0+1+2. For example, at around 130ms, an opposite trend in the thrust plot is evident: dynamics from modes 0+1+2 generate thrust, whereas the resulting kinematics due to combination of modes 0+1 only show the evidence of a drag force. Also, the lift curve associated with modes 0+1 falls below that of modes 0+1+2 and the first 7 modes, indicating a lower mean lift. This is remarkable because the only difference is mode 2, which contributes less than 1% to the overall kinematics, or ~20% if the rigid translational motion is excluded.

C. Flow field analysis

The flow field evolution for one cycle (50ms – 183ms) for modes 0+1 and modes 0+1+2 are discussed below. Three vertical planes normal to the y axis are used to better illustrate the pressure contours around the wing. For modes 0+1, Figure 8–Figure 10 show the temporal evolution of pressure contours around the wing at $y = 1.5$, $y = 1.65$ and $y = 1.8$ planes, respectively. Similarly, Figure 11–Figure 13 describe the pressure contours for modes 0+1+2 at the same three locations. Note that $t = 0$ to 1 is used to indicate the nondimensional time period, where $t = 0$ represents the beginning of the upstroke at 50ms, and $t = 1$ represents the end of the downstroke at 183ms. The presence of an LEV or a TEV will be manifested in the form of a low pressure region.

1) Modes 0 + 1

For modes 0+1, from $t = 0.1 - 0.2$, an LEV is generated that grows in strength on the ventral side of the leading edge. By comparing Figure 8–Figure 10 at the same time instants, we can see that its strength also increases towards the wingtip. This low pressure region is reflected in Figure 7 (1), in the middle of the upstroke (60ms – 80ms), where a large negative lift force can be observed, with a positive thrust as the wing is slightly pitching up.

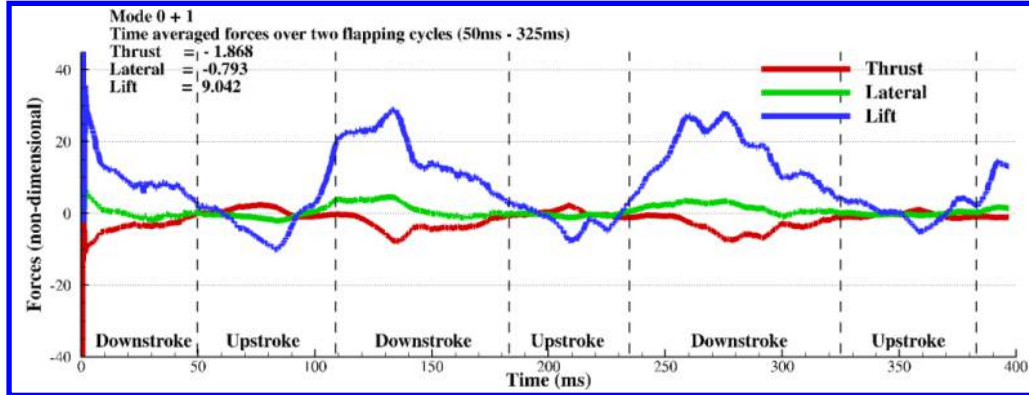
From $t = 0.3$, the LEV starts to separate from the ventral side of the leading edge and as a result, the thrust becomes smaller and the negative lift is alleviated.

The upstroke ends at around $t = 0.4$, when the LEV completely separates from the leading edge and dissipates quickly downstream. It begins to form on the dorsal side of the wing, and a positive lift is thus observed. At the same time, the thrust is small because the wing is not pitched.

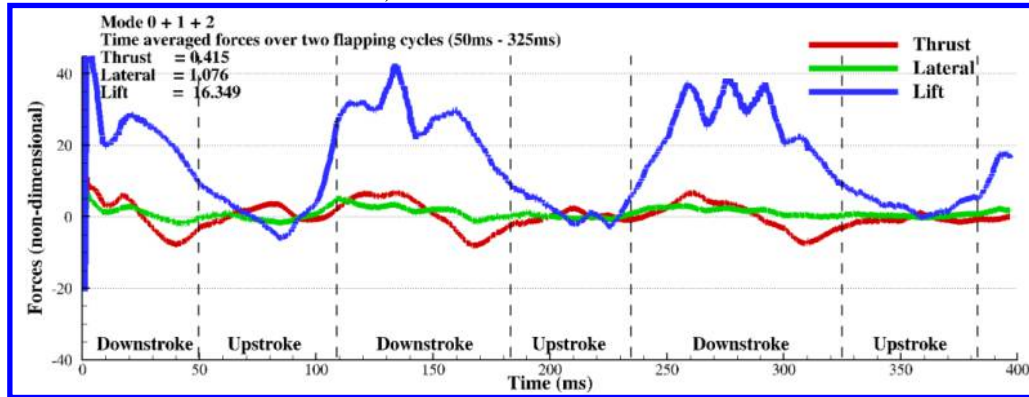
At the beginning of the downstroke around $t = 0.5$, a TEV separates from the dorsal side of the wing and is convected downstream. In the meantime, a large LEV starts to form on the dorsal side of the wing. Because the wing is slightly pitching up with a low pressure region on the dorsal side, drag is produced, as well as a large lift force.

The wing continues to move downward at $t = 0.6$. While the LEV gains strength across the span, comparing Figure 8–Figure 10, we see that the outer part of the wing grows faster. As a result, the low pressure region almost covers the entire dorsal side of the wing, and a peak lift is observed, while at the same time, because the wing has a large positive pitching angle, a large drag is also produced.

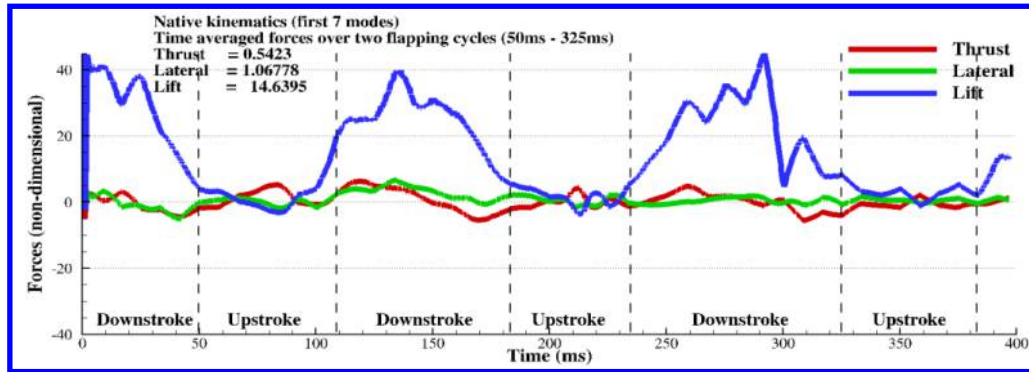
Past $t = 0.6$, this large LEV becomes unstable, and between $t = 0.7 - 0.8$, the separation of the LEV starts from the outer part of the wing. As a result, the low pressure region starts to move away from the dorsal side of the wing, thus the lift is seen to drop, as well as the drag force.



1) Force evolution for modes 0 + 1



2) Force evolution for modes 0 + 1 + 2



3) Force evolution for the first 7 modes (native kinematics)

Figure 7. Force history associated with different POD mode combinations.

From $t = 0.9 - 1.0$, the LEV separates completely, and becomes part of the wake, as the wing slows down to commence the next upstroke.

4) Modes 0+1+2

For modes 0+1+2, at the beginning of the upstroke, at around $t = 0 - 0.1$, the wing does not intersect with any of the cut planes as it is folded inward.

From $t = 0.1 - 0.2$, the wing is seen to have a large positive pitching angle and is almost vertically positioned. As a result, though no LEV is formed, a low pressure region is still observed on the ventral side of the wing which contributes to the thrust.

At around $t = 0.2$, the trailing edge of the wing is seen to be interacting with the wake structure from the previous downstroke. Comparing Figure 11-Figure 13, the interaction is more pronounced in the inner part of the wing. The wing is seen to be experiencing a fast rotation, and an LEV starts to form, as a result, the negative peak lift and thrust are observed.

At around $t = 0.3$, this LEV stays attached even though the wing is continuously rotating. As a result, the wing is able to escape the wake from the previous downstroke, and starts to generate lift. Because the wing is almost horizontal now, the thrust is not as pronounced.

At the end of upstroke, at around $t = 0.4$, a TEV can be seen and the wing is already generating lift as the low pressure region has covered the entire dorsal side of the wing. Comparing with Figure 11-Figure 13, it can also be seen that the TEV grows in strength along the span.

As the wing starts to move downward, at $t = 0.5-0.6$, the TEV is no longer stable and starts to separate from the dorsal side. In the meantime, an LEV starts to form and grows in strength along the span (Figure 11-Figure 13). As a result, these two counter rotating vortices creates a stagnation region with high pressure at the middle of the wing, and lift is seen to drop. Quite remarkably, the wing has slightly pitched downward and as a result, the thrust is produced instead of drag similar to modes 0+1.

From $t = 0.7 - 0.8$, a part of the TEV on the dorsal side of the wing rolls towards the ventral side, thus effectively reducing the high pressure region on the ventral side of the wing decreasing lift. At the same time, the wing is rapidly pitching upward and as a result, drag is produced.

At $t = 0.9$, the wing is highly cambered, as well as in rapid upward pitching. The LEV starts to separate from the dorsal side of the wing starting at the outer part of the wing.

Finally, at $t = 1$, the wing is seen to fold inward, to get ready for the next upstroke.

5) Key comparison between modes 0+1 and modes 0+1+2

For both combinations, quite remarkably, towards the end of upstroke, lift is already positive, in other words, lift is also generated during the upstroke for both cases, which was also observed in Viswanath *et al.*²⁸ On closer examination, we noticed that the rotation speed of the wing is small, as the wing is getting ready for the downstroke, resulting in smaller instantaneous unsteadiness levels. In other words, the flow around the wing during that short amount of time could be assumed to be steady around a stationary wing (there is no wake interaction), and because the wing in both cases has a positive curvature, pressure becomes smaller on the dorsal side for both cases just like in a conventional airfoil.

There are two time periods that highlight the importance of mode 2:

Between $t = 0-0.3$, the orientation of the wing plays a crucial role in thrust and lift generation; with mode 2 included, the wing not only mitigates the peak negative lift compared to modes 0+1, it also harvests the LEV on the ventral side to produce thrust. The outer part of the wing also generates more thrust per area due to a more favorable orientation.

Between $t = 0.5-0.8$, the orientation of the wing plays a crucial role in lift generation; with mode 2 included, the LEV tends to grow and stay attached on the dorsal surface, generating substantially more lift.

E. Conclusion

In this work, we have identified two modes (1 and 2) of the bat wing kinematics that are essential for the generation of lift and thrust. Mode 1 acts like a rigid flapping wing in place, and mode 2 provides the wing with extra spanwise and chordwise cambering. Subsequently, we simulated three cases using motion prescribed by mode combinations (modes 0+1+2, modes 0+1+2 and modes 0+1+2+3+4+5+6). The results show that by recovering modes 1 and 2, the aerodynamic forces are nearly identical with those generated by the full motion. This can provide guidelines for the design of flapping wing MAV where a good trade-off between motion complexity and overall performance is constantly desired. Detailed flow field analyses for modes 0+1 and modes 0+1+2 revealed that the addition of mode 2 has two major effects: 1) during the upstroke, the wing is pitched up, which alleviates the negative lift, 2) during the

downstroke, the slight downward pitching makes the wing generate thrust instead of drag and the LEV stays attached on the dorsal side longer, thus generating more lift.

Acknowledgments

The financial support of the NSF CBET Grant No. 1510797, NSF IRES Grant No. 1658620, support from VT ICTAS/BIST Center, National Natural Science Foundation of China (Grant Nos. 11374192 & 11574183), Chinese Ministry of Education Tese Grant for international faculty exchange is gratefully acknowledged. The authors would also like to acknowledge support fi from the SDU-VT International Lab at Shandong University and the computational resources provided by Advanced Research Computing (ARC) at Virginia Tech.

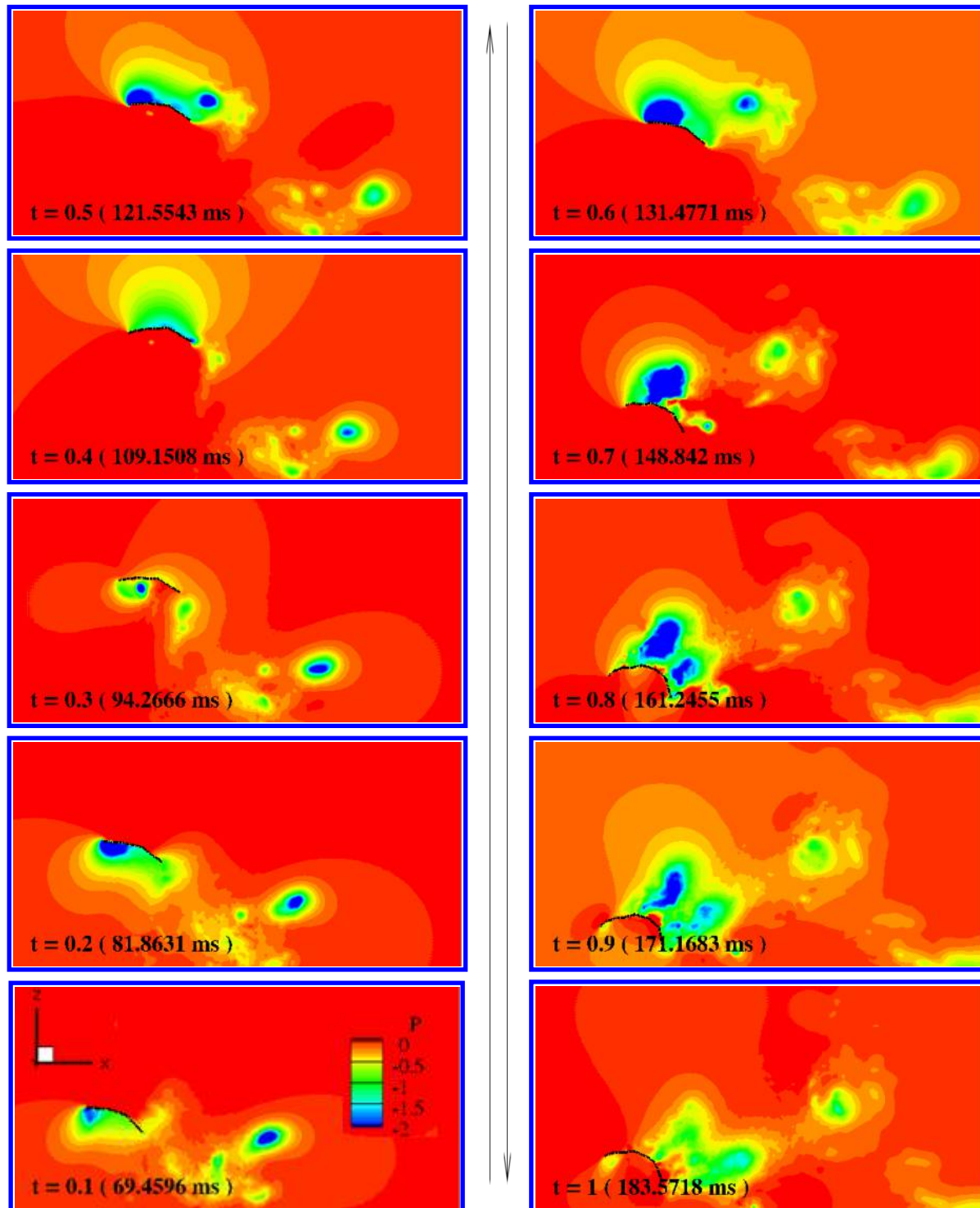


Figure 8. Pressure contours for modes 0 + 1 in vertical y-plane at $y = (43\%$ of maximum span length). View is from left wing to right wing and flow direction is in the positive x – direction.

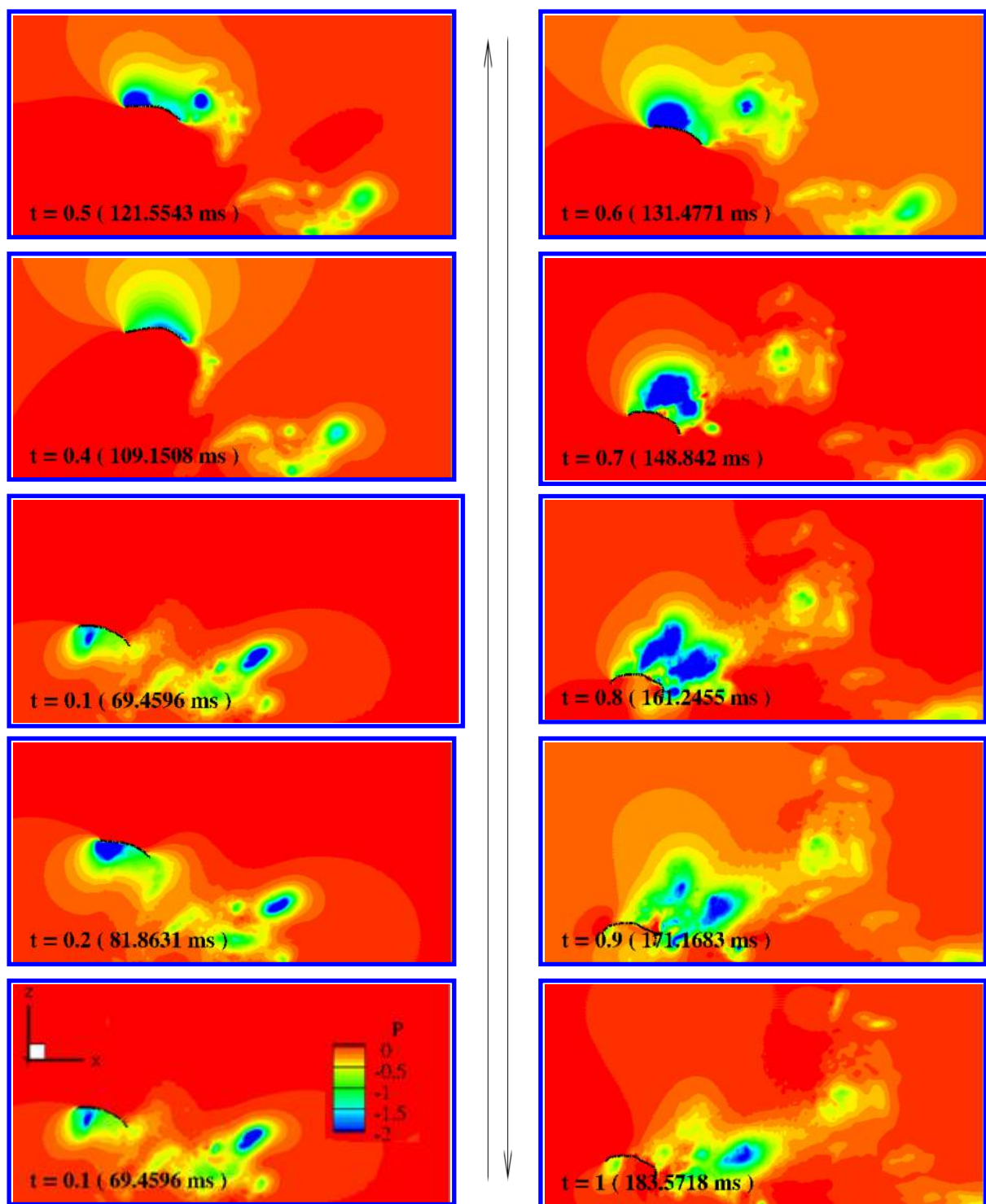


Figure 9. Pressure contours for modes 0 + 1 in vertical y-plane at $y = (47\%$ of maximum span length). View is from left wing to right wing and flow direction is in the positive x – direction.

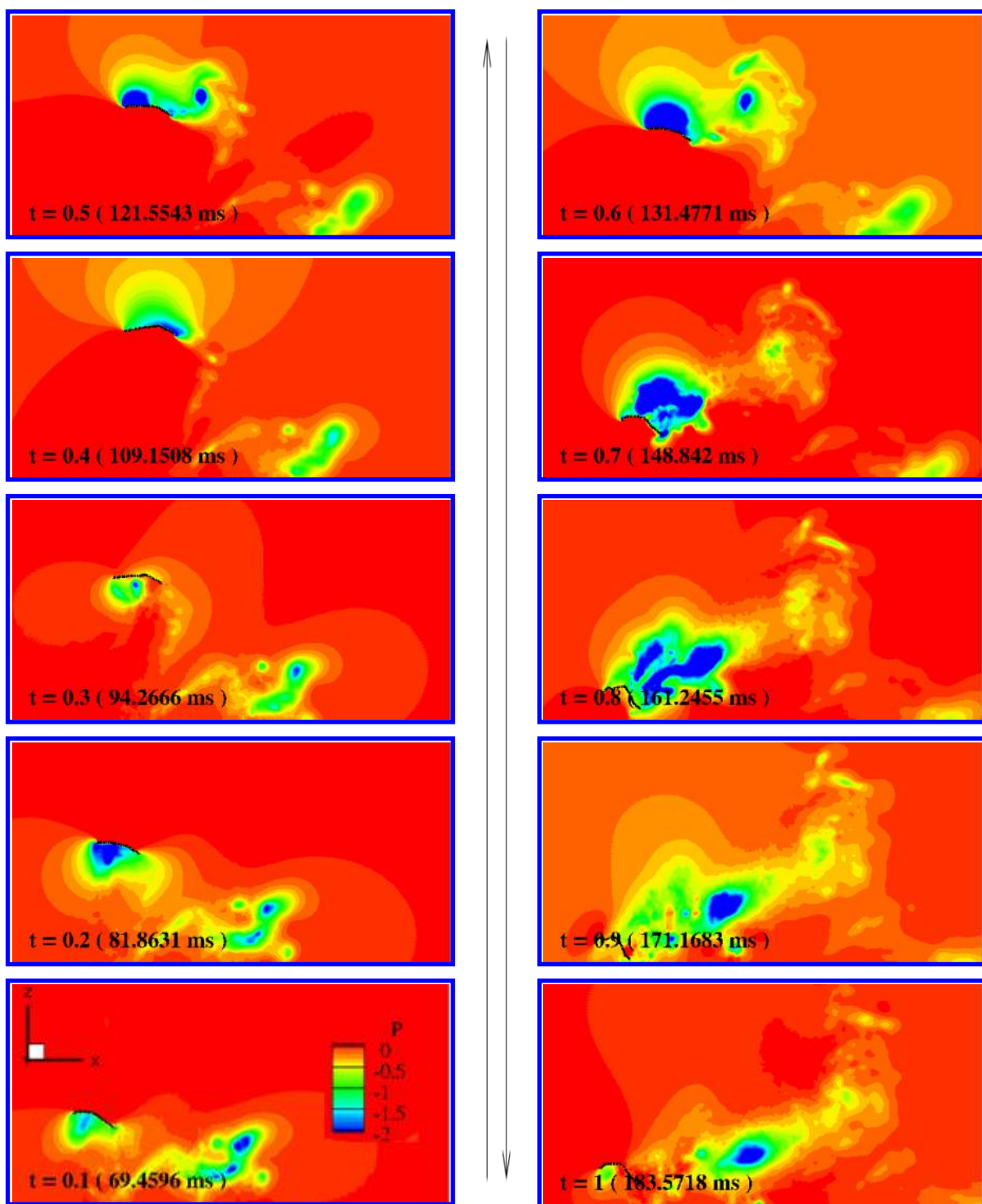


Figure 10. Pressure contours for modes 0 + 1 in vertical y-plane at $y = (51\%$ of maximum span length). View is from left wing to right wing and flow direction is in the positive x – direction.

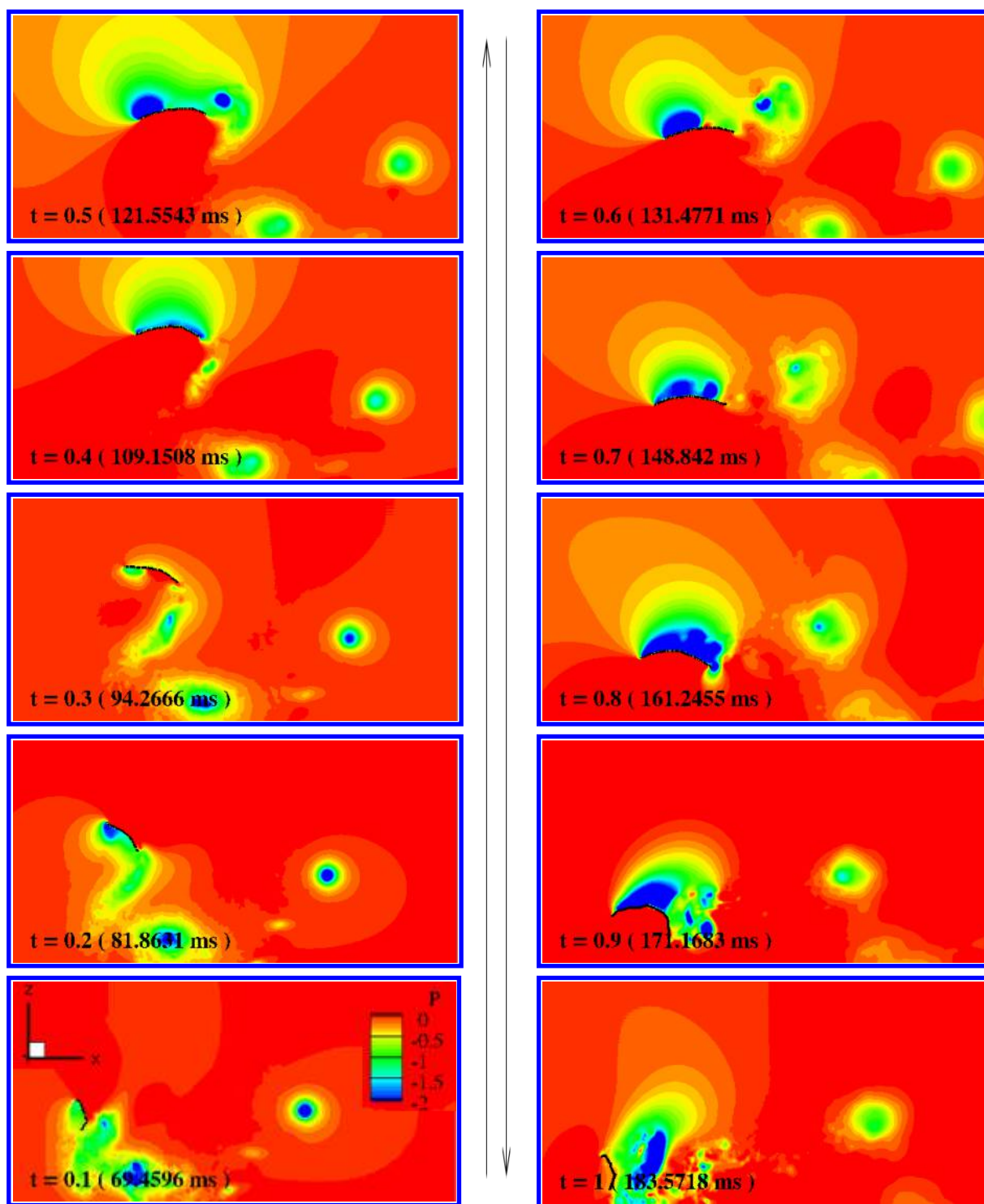


Figure 11. Pressure contours for modes 0 + 1 + 2 in vertical y-plane at $y = (43\% \text{ of maximum span length})$. View is from left wing to right wing and flow direction is in the positive x – direction.

a) Modes 0 + 1 + 2

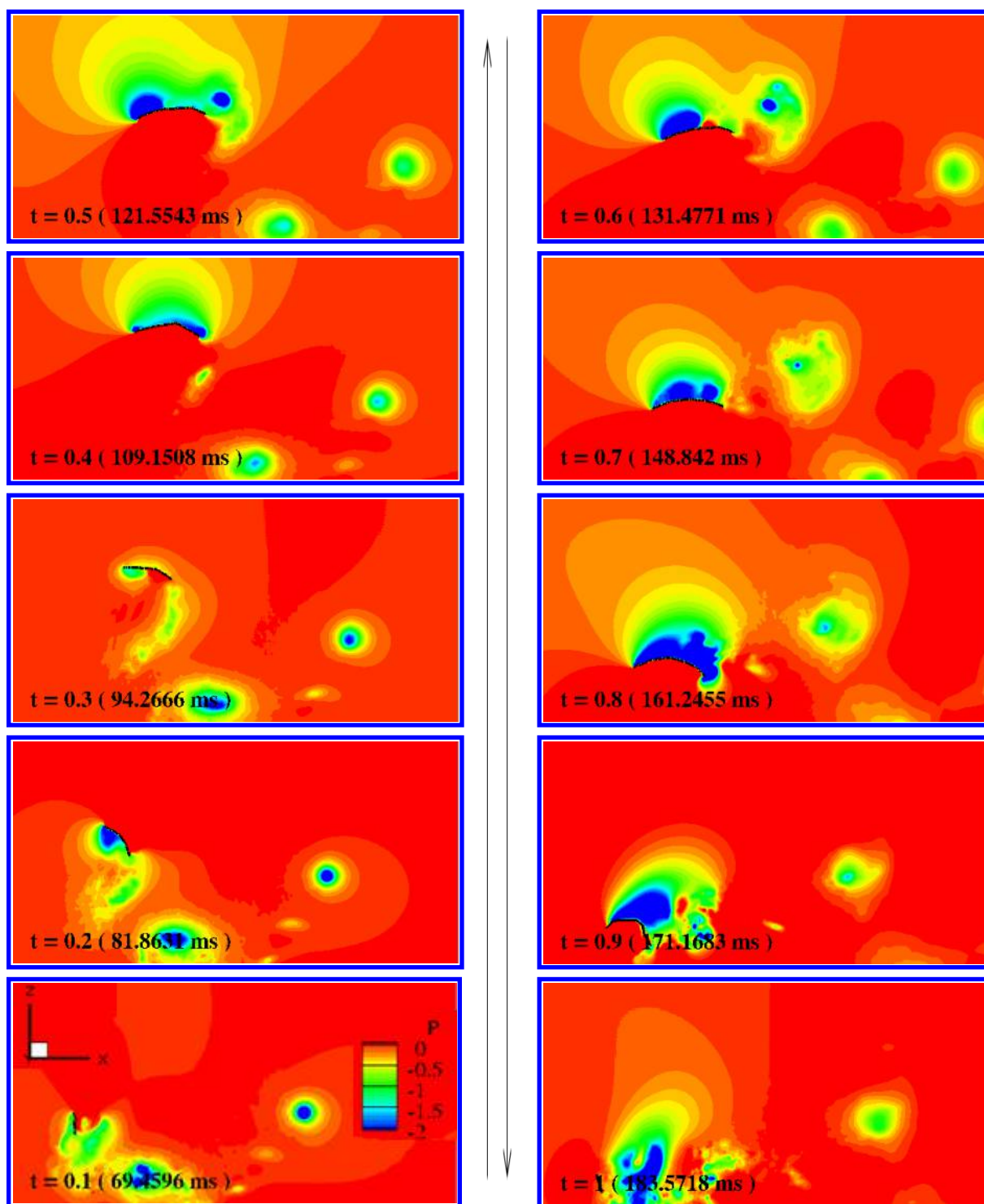


Figure 12. Pressure contours for modes 0 + 1 + 2 in vertical y-plane at $y = (47\% \text{ of maximum span length})$. View is from left wing to right wing and flow direction is in the positive x – direction.

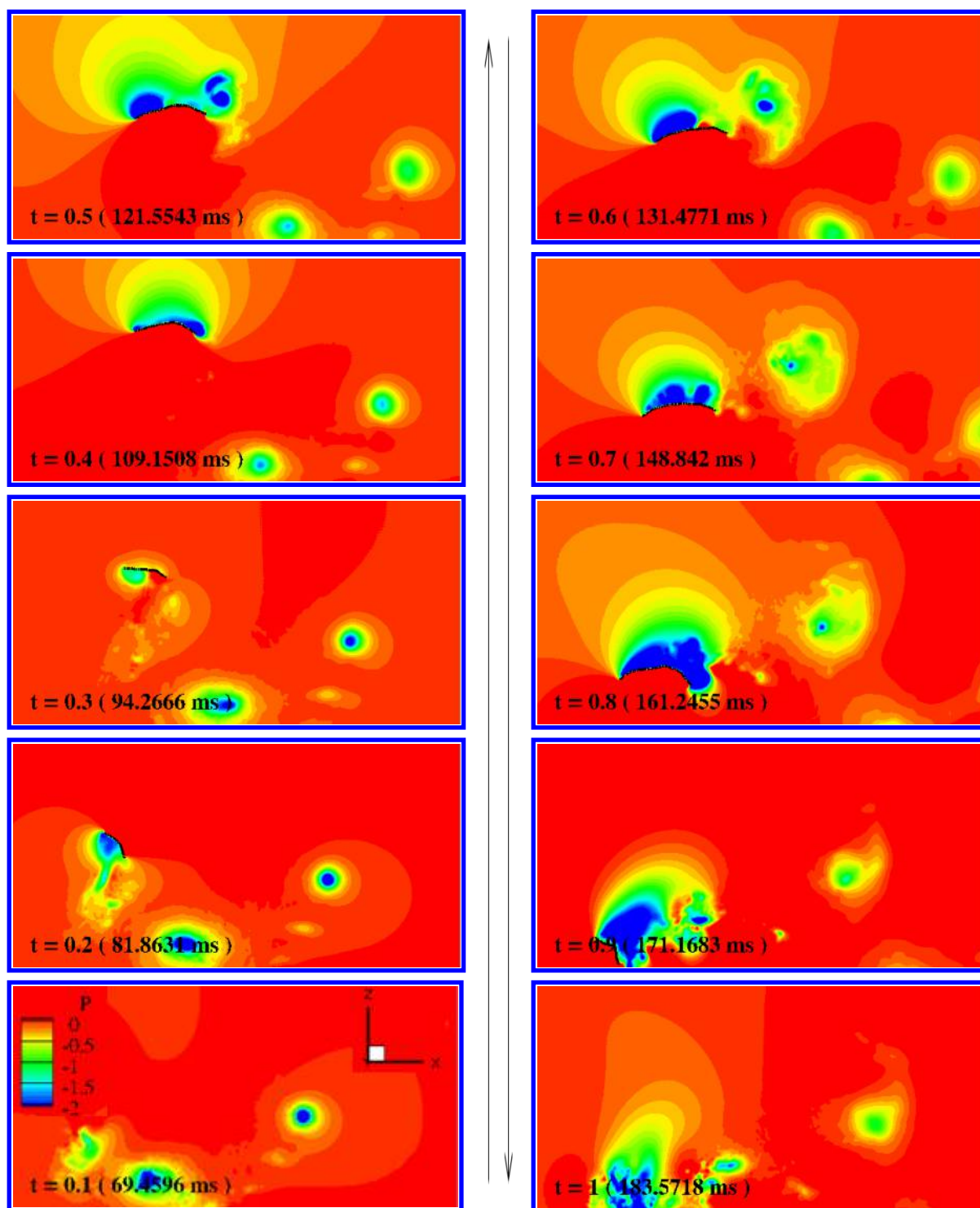


Figure 13. Pressure contours for modes 0 + 1 + 2 in vertical y-plane at $y = (51\% \text{ of maximum span length })$. View is from left wing to right wing and flow direction is in the positive x – direction.

References

- ¹ Hedenström, A., Johansson, L. C., and Spedding, G. R., "Bird or bat: comparing airframe design and flight performance," *Bioinspiration & Biomimetics*, vol. 4, 2009, p. 15001.
- ² Cheney, J. A., Konow, N., Middleton, K. M., Breuer, K. S., Roberts, T. J., Gibling, E. L., and Swartz, S. M., "Membrane muscle function in the compliant wings of bats," *Bioinspiration & Biomimetics*, vol. 9, 2014, p. 25007.
- ³ Gerdes, J. W., Gupta, S. K., and Wilkerson, S. A., "A Review of Bird-Inspired Flapping Wing Miniature Air Vehicle Designs," *Journal of Mechanisms and Robotics*, vol. 4, 2012, p. 21003.
- ⁴ Ma, Y. K., Chirarattananon, P., Fuller, B. S., and Wood, J. R., "Controlled Flight of a Biologically Inspired, Insect-Scale Robot," *Science*, 2013, pp. 603–607.
- ⁵ Chung, S.-J., and Dorothy, M., "Neurobiologically Inspired Control of Engineered Flapping Flight," *Journal of Guidance, Control, and Dynamics*, vol. 33, 2010, pp. 440–453.
- ⁶ Ramezani, A., Chung, S.-J., and Hutchinson, S., "A biomimetic robotic platform to study flight specializations of bats," *Science Robotics*, vol. 2, 2017, p. eaal2505.
- ⁷ Lentink, D., Jongerius, S. R., and Bradshaw, N. L., "The scalable design of flapping micro-air vehicles inspired by insect flight," *Flying Insects and Robots*, 2010, pp. 185–205.
- ⁸ Nakata, T., Liu, H., Tanaka, Y., Nishihashi, N., Wang, X., and Sato, A., "Aerodynamics of a bio-inspired flexible flapping-wing micro air vehicle," *Bioinspiration & Biomimetics*, vol. 6, 2011, p. 45002.
- ⁹ Bender, M. J., McClelland, H. G., Bledt, G., Kurdila, A., Furukawa, T., and Mueller, R., "Trajectory Estimation of Bat Flight Using a Multi-View Camera System," *Modeling and Simulation Technologies Conference, SciTech 2015*, 2015, pp. 1–13.
- ¹⁰ Tian, X., Iriarte-Diaz, J., Middleton, K., Galvao, R., Israeli, E., Roemer, A., Sullivan, A., Song, A., Swartz, S., and Breuer, K., "Direct measurements of the kinematics and dynamics of bat flight," *Bioinspiration & Biomimetics*, vol. 1, 2006, pp. S10–S18.
- ¹¹ Hedenstrom, A., and Johansson, L. C., "Bat flight: aerodynamics, kinematics and flight morphology," *Journal of Experimental Biology*, vol. 218, 2015, pp. 653–663.
- ¹² Muijre, F.T.(Department of Theoretical Ecology, L. U., "Leading-Edge Vortex Improves Lift in Slow-Flying Bats," *Science*, vol. 319, 2006, p. 1250.
- ¹³ Hubel, T. Y., Riskin, D. K., Swartz, S. M., and Breuer, K. S., "Wake structure and wing kinematics: the flight of the lesser dog-faced fruit bat, *Cynopterus brachyotis*," *Journal of Experimental Biology*, vol. 213, 2010, pp. 3427–3440.
- ¹⁴ Hubel, T. Y., Hristov, N. I., Swartz, S. M., and Breuer, K. S., "Wake structure and kinematics in two insectivorous bats," *Philosophical Transactions of the Royal Society B: Biological Sciences*, vol. 371, 2016, p. 20150385.
- ¹⁵ Bender, M. J., McClelland, H. M., Kurdila, A., and Mueller, R., "Recursive Bayesian Estimation of Bat Flapping Flight Using Kinematic Trees," *AIAA Modeling and Simulation Technologies Conference*, 2016, pp. 1–12.
- ¹⁶ Pivkin, I. V., Hueso, E., Weinstein, R., Laidlaw, D. H., Swartz, S., and Karniadakis, G. E., "Simulation and Visualization of Air Flow Around Bat Wings During Flight," *Lncs*, vol. 3515, 2005, pp. 689–694.
- ¹⁷ Wang, S., Zhang, X., He, G., and Liu, T., "Numerical simulation of unsteady flows over a slow-flying bat," *Theoretical and Applied Mechanics Letters*, vol. 5, 2015, pp. 5–8.
- ¹⁸ Viswanath, K., "Effect Of Frontal Gusts And Stroke Deviation In Forward Flapping Flight And Deconstructing The Aerodynamics Of A Fruit Bat," *Ph.D. Thesis, Department of Mechanical Engineering, Virginia Polytechnic Institute and State University*, 2013, p. 144.
- ¹⁹ R., J., and de Boor, C., "A Practical Guide to Splines," *Mathematics of Computation*, vol. 34, 1980, p. 325.
- ²⁰ Folch-Fortuny, A., Arteaga, F., and Ferrer, A., "Missing Data Imputation Toolbox for MATLAB," *Chemometrics and Intelligent Laboratory Systems*, vol. 154, 2016, pp. 93–100.
- ²¹ Kerschen, G., Golinval, J. C., Vakakis, A. F., and Bergman, L. A., "The method of proper orthogonal decomposition for dynamical characterization and order reduction of mechanical systems: An overview,"

- 22 *Nonlinear Dynamics*, vol. 41, 2005, pp. 147–169.
- 23 Riskin, D. K., Willis, D. J., Iriarte-Díaz, J., Hedrick, T. L., Kostandov, M., Chen, J., Laidlaw, D. H., Breuer, K. S., and Swartz, S. M., “Quantifying the complexity of bat wing kinematics,” *Journal of Theoretical Biology*, vol. 254, 2008, pp. 604–615.
- 24 Tafti, D. K., “GenIDLEST: A scalable parallel computational tool for simulating complex turbulent flows,” *ASME-PUBLICATIONS-FED*, 2001, pp. 347–356.
- 25 Tafti, D. K., *6 Time-accurate techniques for turbulent heat transfer analysis in complex geometries*, 2010.
- 26 Viswanath, K., Nagendra, K., Cotter, J., Frauenthal, M., and Tafti, D. K., “Straight-line climbing flight aerodynamics of a fruit bat,” *Physics of Fluids*, vol. 26, 2014.
- 27 Germano, M., Piomelli, U., Moin, P., and Cabot, W. H., “A dynamic subgrid-scale eddy viscosity model,” *Phys. Fluids A Fluid Dyn.*, vol. 3, 1991, p. 1760.
- 28 Nagendra, K., Tafti, D. K., and Viswanath, K., “A new approach for conjugate heat transfer problems using immersed boundary method for curvilinear grid based solvers,” *Journal of Computational Physics*, vol. 267, 2014, pp. 225–246.
- Viswanath, K., and Nagendra, K., “Climbing Flight of a Fruit Bat Deconstructed,” *52nd Aerospace Sciences Meeting, 13-17 January 2014*, 2014, pp. 1–24.